www.adeepakpublishing.com

Omar, S. R. et al. (2021): JoSS, Vol. 10, No. 1, pp. 943–957
(Peer-reviewed article available at www.jossonline.com)

www. JoSSonline.com

The Drag Maneuvering Device for the Semi-Passive Three-Axis Attitude Stabilization of Low Earth Orbit Nanosatellites

Sanny R. Omar, Camilo Riano-Rios, and Riccardo Bevilacqua

University of Florida
Advanced Autonomous Multiple Spacecraft Lab
Gainesville, FL US

Abstract

The increase in use of small satellites since their initial development has led to many missions with simple attitude and orbit control requirements. For example, a small Earth-imaging satellite may require keeping one face nadir pointing within 10 degrees while maintaining a slot in a low Earth orbit within ±100 km. However, legacy attitude and orbit control techniques, including reaction wheels and thrusters, can easily cost tens of thousands of dollars and provide more control capability than is needed for such a mission.

This paper introduces a Drag Maneuvering Device (DMD) that could replace such systems on many missions. Consisting of four retractable tape spring booms deployed in a dart configuration, the DMD can actively modulate the drag area of the host satellite for orbital maneuvering and post-mission disposal while providing passive three-axis attitude stability, using aerodynamic and gravity gradient torques. Magnetorquers integrated into the DMD damp attitude oscillations and help ensure that the satellite stabilizes with the correct face nadir pointing. The current study provides an overview of the DMD design and details the results of the attitude and orbit simulations used to characterize the DMD performance and devise a control and operations methodology. Emphasis is placed on the attitude stability properties of the DMD in this work.

1. Introduction

Attitude and orbit control have been important considerations since the early days of space exploration (Roberson, 1979). Traditionally, attitude control has been performed using reaction wheels (Steyn and Hashida, 1999), control moment gyros, and thrusters; and orbit control has been performed using thrusters (Curtis, 2009; Markley and Crassidis, 2014). These legacy attitude and orbit control systems have been complicated and expensive, but they are also highly accurate and capable of rapid response, making them well-suited to large, high-budget satellite missions. Three-axis attitude control systems have been developed for small satellites such as CubeSats in recent years (Heidt et al., 2000; Mason et al., 2016), but these systems can still cost tens of thousands of dollars. Alternative attitude and orbit control methodologies using environmental forces and torques have been proposed (Shrivastava and Modi, 1983), and

Corresponding Author: Sanny Omar – sanny.omar@gmail.com
Publication History: Submitted – 01/02/20; Accepted – 12/28/20; Published: 02/26/21

have become particularly valuable in recent years with the introduction of small satellites that lack the volume, power, or budget for legacy systems.

Aerodynamic drag force is a naturally occurring effect that is dependent on the satellite's orientation, geometry, and orbital regime (Shrivastava and Modi, 1983). Aerodynamic drag has been used for orbital maneuvering, and methods for using aerodynamic torques for attitude control have been investigated in prior literature (Pastorelli et al., 2015). Gravity gradient torques are dependent on the spacecraft moments of inertia, and can also be harnessed for attitude stabilization through the use of a gravity gradient boom (Arduini and Baiocco, 1997; Curtis, 2009). In low Earth orbit, electromagnets (called magnetorquers) embedded in the satellite can interact with the Earth's magnetic field to impart torques on the satellite. Magnetorquers have commonly been used for detumble and for reaction wheel desaturation (Silani and Lovera, 2005). The ZA-AeroSat CubeSat (Steyn and Kearney, 2014) used a passively aerodynamically stable spacecraft design in tandem with magnetorquers and a single momentum wheel in a y-Thompson spin configuration to provide attitude stability. A gravity gradient boom was employed by the UOSAT-2 mission along with magnetorquers to perform two-axis attitude stabilization with one axis nadir-pointing (Hodgart, 1989).

Though environmental torques have been used on prior satellite missions for attitude control, and various control solutions have been investigated in the literature, most current solutions either do not provide three-axis attitude control or require additional actuators, like thrusters or wheels, to provide complete control that is robust and reliable. Methods that do investigate three-axis attitude control generally require costly sensors to provide three-axis attitude determination. At a minimum, Kalman filtering of magnetometer measurements is needed, coupled with knowledge of the spacecraft's position and the Earth's magnetic field at that position to determine the spacecraft's attitude (Hodgart, 1989). This imposes an additional computational burden and requires precise magnetometer calibration and a means of satellite position determination. Techniques that use aerodynamic torques for ram-alignment (Pastorelli et al., 2015), gravity gradient torques for zenith alignment (Arduini and Baiocco, 1997), or magnetic torques for magnetic field alignment (Kumar et al., 1995) all leave one axis of rotation unconstrained.

To date, there is no device or control solution to the authors' knowledge that facilitates aerodynamically-based orbital maneuvering while enabling three-axis attitude stabilization using environmental torques without the need for attitude determination.

This paper introduces a Drag Maneuvering Device (DMD) that provides such an attitude and orbit control solution. While the use of aerodynamic, gravity gradient, and magnetic torques to facilitate attitude stability is not itself a novel concept, the combined use of these torques by the DMD for semi-passive three-axis attitude stability is. The DMD uses aerodynamic torques to align the z-axis (see Figure 1) with the velocity direction, while simultaneously generating a gravity gradient effect through differential boom deployment to align an axis in the x-y plane with the nadir vector. Fully and partially deployed DMDs integrated into two-unit (10 x 10 x 23 cm) CubeSats are shown in Figure 2.

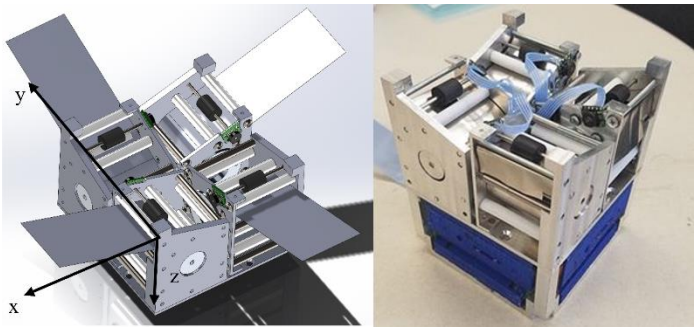

Figure 1. Drag Maneuvering Device (DMD) CAD model and prototype.

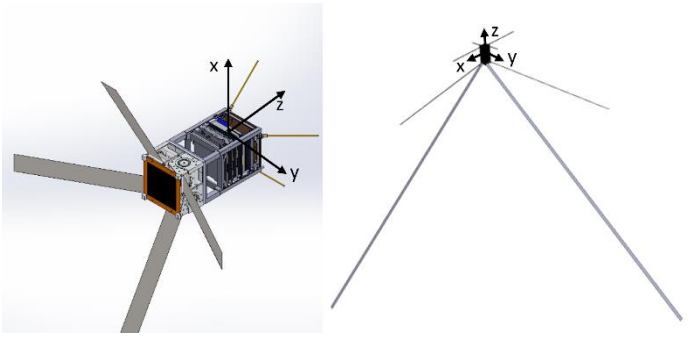

Figure 2. Partially and fully deployed DMD mounted on a 2U CubeSat.

Use of only gravity gradient effects would allow an unconstrained rotation about the nadir-pointing axis (Hodgart, 1989), while use of solely aerodynamic effects would allow an unconstrained rotation about the ram-aligned axis (Underwood et al., 2019). However, use of both effects simultaneously creates an equilibrium condition with all three axes constrained. To aid in the attitude stabilization, the magnetorquer BDot de-tumble controller (Lovera, 2015) can be used, which does not require magnetometer calibration or knowledge of the satellite's position. To the author's knowledge, no other such device exists that provides this kind of semi-passive, three-axis attitude stability without the need for attitude determination, wheels, or thrusters. The design, operation, and control methodology behind the DMD are discussed in this paper, and a 6DOF (degree of freedom), high fidelity attitude and orbit model is introduced to verify the semi-passive, three-axis attitude stability properties of the DMD.

2. Drag Maneuvering Device (DMD) Design

The Drag Maneuvering Device (DMD), formerly called the Drag De-Orbit Device (D3) (Guglielmo et al., 2019), consists of four tape spring booms, each 3.7 m long and 4 cm wide, inclined at a 20-degree angle relative to the face of the satellite to which the DMD is attached (x-y plane), as shown in Figures 1 and 2. The booms are deployed in this shuttlecock configuration to provide passive aerodynamic attitude stability. Three magnetorquers (one along each axis) are wrapped around the blue 3D-printed brackets shown in the right-side image in Figure 1 to aid in attitude stabilization. Depending on the structure of the host CubeSat and the presence of magnetorquers elsewhere on the satellite, the DMD can optionally be built without the adapter stage and magnetorquers, reducing its length in the z-direction from 11.3 cm to 7 cm. Because the torques acting on the DMD system will be small (micro-Newton-meters) and of a low frequency, these torques are not expected to induce significant boom oscillations. Additionally, one pair of opposing booms can be partially retracted while the other pair is fully deployed, to create a minimum moment of inertia axis along the direction of the deployed booms. Gravity gradient torques will then work to passively align this axis with the nadir or zenith vector. Running the BDot de-tumble law (Arduini and Baiocco, 1997) using magnetorquers embedded in the DMD serves to damp initial satellite rotation rates and the attitude oscillations that will persist after boom deployment. The combination of aerodynamic, gravity gradient, and magnetic torques generated by the DMD provide three-axis attitude stabilization and ensure that a single face of the satellite is pointing toward Earth with negligible power usage after the initial detumble and stabilization.

As a bonus, the DMD booms can be collectively deployed or retracted to vary the cumulative aerodynamic drag experienced by the satellite, which can be used for orbital maneuvering, constellation phasing, collision avoidance, and controlled re-entry (Omar and Bevilacqua, 2019). No other device, to the author's knowledge, leverages both aerodynamic and gravity gradient torques to provide three-axis attitude stabilization with no unconstrained axis of rotation. In addition, because the BDot magnetorquer control law is the only active control utilized during the attitude stabilization, complete attitude determination is not necessary. This greatly simplifies the control logic and eliminates the need for magnetometer calibration, position knowledge, or onboard lookup tables with magnetic field information such as the IGRF (International Geomagnetic Reference Field) (Thébault et al., 2015). Each DMD deployer (Figure 3) contains a brushed DC motor (Faulhaber 1516-006SR with 262:1 spur gearbox) that drives a drum to which a boom is connected. As the motor rotates, the boom extends and drives a silicone roller attached to the shaft of a rotary encoder that precisely measures the amount of boom deployment.

The DMD attaches to a host CubeSat via a structural interface adapter that also contains magnetorquers wrapped around 3D-printed Ultem brackets (brackets in blue in Figure 4). The DMD with adapter weighs approximately 1.3 kg, increases the undeployed size of the host satellite by 1U (10 x 10 x 11.35 cm), and increases the drag area by up to .5 m^2. Figure 4 shows a DMD prototype with magnetorquer brackets 3D-printed in blue attached to a 1U CubeSat structure to conform to the 2U (10 x 10 x 22.7 cm) CubeSat form factor.

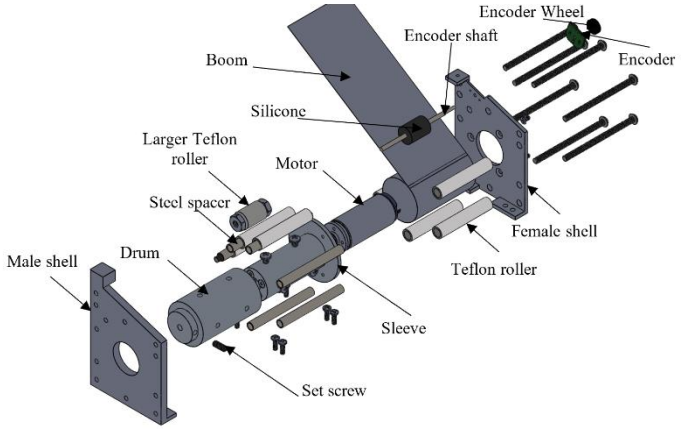

Figure 3. DMD deployer expanded view.

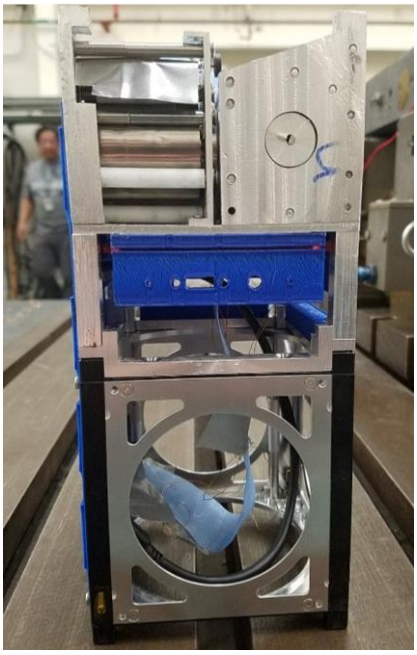

Figure 4. Prototype of DMD with CubeSat structure.

A key benefit of the DMD is its low cost, ease of assembly, and ease of operations compared with traditional wheel-based, three-axis attitude control systems. The cost to professionally manufacture or procure off-the-shelf all DMD components is less than $5,000 USD. All machined DMD components were designed to be manufacturable with the capabilities of the average university machine shop, which reduces the cost of the DMD hardware to under $2,000 USD. Approximately one week of full-time work is required for a student with a typical undergraduate engineering education to assemble and test the DMD. Though the DMD may appear more mechanically complex than a reaction wheel system, it does not require the complex interplay between sensors, estimators, controllers, and actuators associated with a traditional ADCS system that typically takes a team of highly skilled GNC engineers to perfect. It is for this reason that wheel-based ADCS units for CubeSats usually cost tens of thousands of dollars and are generally beyond the scope of what a university team or an inexperienced company can produce (see Table 1).

The mechanical functionality of DMD boom deployment, in contrast, can be fully verified on the ground and does not require the expertise to assemble or test that is needed for conventional ADCS systems. Prior laboratory tests conducted on a DMD deployer prototype (Guglielmo et al., 2019) showed the deployer capable of performing 500 deploy-retract cycles with no jams or hang-ups, giving confidence that the system will perform without failure in space. The BDot magnetorquer control law is among the simplest of ADCS algorithms and is

Table 1. DMD Compared to Legacy ADCS Solutions (Small Spacecraft Systems Virtual Institute, 2020)

	DMD	BCT XACT-15[1]	MAI-400[2]	CubeSpace CubeADCS[3]
Cost[4]	$2k-$5k	$100k+	$50k+	$37.4k
Pointing error	<20 deg, 6 deg expected	.007 deg	1 deg	1 deg
Steady state power draw	0 (passive)	<4.0 W	1.1W	1.0 W
Manufacturable at university	Yes	No	No	No

[1] https://bluecanyontech.com/components
[2] https://www.adcolemai.com/wp-content/uploads/2019/02/AMA-MAI-400-Datasheet.pdf
[3] https://www.cubespace.co.za/products/integrated-adcs/3-axis/
[4] BCT XACT and MAI-400 approximate costs based on unofficial conversations with vendors and CubeSat builders

within the capability of an undergraduate student in engineering to implement. The low cost and relative simplicity of building, testing, and operating the DMD make it well suited for university CubeSat projects where a satellite face must remain nadir-pointing for communication or science purposes but precise attitude control is not required. Small companies without significant GNC expertise that are looking to build low-cost satellites without strict attitude control requirements may also benefit from the DMD. Table 1 provides a comparison of DMD cost, performance, and properties to those of off-the-shelf ADCS units currently available for CubeSats.

3. Attitude and Orbit Simulation Framework

To simulate the attitude and orbital dynamics of the satellite, a six-degree-of-freedom numerical attitude and orbit propagator was created. The satellite state vector was $\boldsymbol{x} = [\boldsymbol{r^T} \quad \boldsymbol{v^T} \quad \boldsymbol{q^T} \quad \boldsymbol{\omega^T}]^T$, where $\boldsymbol{r}$ is the satellite position vector in the ECI (Earth Centered Inertial) frame, $\boldsymbol{v}$ is the ECI velocity vector, $\boldsymbol{\omega}$ is the angular velocity of the satellite body frame with respect to the ECI frame, and $\boldsymbol{q}$ is the quaternion defining the rotation from the ECI frame to the satellite body frame. The variable $\boldsymbol{q}$ is defined by Crane and Duffy (2008) and Wie (2008) as:

$$\boldsymbol{q} = \begin{bmatrix} \hat{\boldsymbol{e}} \sin(\theta/2) \\ \cos(\theta/2) \end{bmatrix} = [q_1 \quad q_2 \quad q_3 \quad q_4]^T, \qquad (1)$$

such that a rotation of the ECI frame by angle θ about axis $\hat{\boldsymbol{e}}$ would align it with the spacecraft body frame. At each time step, the state derivative is computed and numerically integrated using the RK78 numerical integration method (Montenbruck and Gill, 2005). The state derivative is calculated as:

$$\dot{\boldsymbol{x}} = [\boldsymbol{v^T} \quad \dot{\boldsymbol{v}}^T \quad \dot{\boldsymbol{q}}^T \quad \dot{\boldsymbol{\omega}}^T]^T, \qquad (2)$$

with the following definitions given by Wie (2008):

$$\dot{\boldsymbol{q}} = \frac{1}{2}\begin{bmatrix} q_4 & -q_3 & q_2 & q_1 \\ q_3 & q_4 & -q_1 & q_2 \\ -q_2 & q_1 & q_4 & q_3 \\ -q_1 & -q_2 & -q_3 & q_4 \end{bmatrix}\begin{bmatrix} \omega_x \\ \omega_y \\ \omega_z \\ 0 \end{bmatrix}, \qquad (3)$$

$$\dot{\boldsymbol{\omega}} = \boldsymbol{J}^{-1}\left(\boldsymbol{\tau_{net}} - \boldsymbol{\omega} \times (\boldsymbol{J\omega})\right), \qquad (4)$$

$$\dot{\boldsymbol{v}} = \frac{\boldsymbol{F_{net}}}{m}. \qquad (5)$$

where $\boldsymbol{J}$ is the satellite moment of inertia about the center of mass, $\boldsymbol{\tau_{net}}$ is the net torque, $\boldsymbol{F_{net}}$ is the net force, and m is the satellite mass. In this study, $\boldsymbol{\tau}_{net}$ is the sum of aerodynamic torque ($\boldsymbol{\tau}_p$), gravity gradient torque ($\boldsymbol{\tau}_{\text{gg}}$), magnetic torque ($\boldsymbol{\tau}_{mag}$), and pseudo-random disturbance torques ($\boldsymbol{\tau}_{dist}$), while $\boldsymbol{F}_{net}$ is the sum of aerodynamic force ($\boldsymbol{F}_p$) and gravitational force ($\boldsymbol{F}_g$). Further, $\boldsymbol{\tau}_{dist}$ captures the torque effects of uncertain parameters such as internal magnetic hysteresis, magnetorquer misalignments, inertia uncertainties, imprecise boom deployment levels, and boom misalignments. It is expected that $\boldsymbol{\tau}_{dist}$ will be significantly smaller in magnitude than the primary torques that are relied upon for spacecraft stability ($\boldsymbol{\tau}_p$, $\boldsymbol{\tau}_{gg}$, and $\boldsymbol{\tau}_{mag}$).

The effects of Earth's non-uniform gravitational field on the orbit are modeled using the EMG2008 gravitational model with spherical harmonics through degree and order ten (Pavlis et al., 2008). The gravitational force, including the most significant perturbation (J_2), can be computed according to Bate et al. (1971) by:

$$\boldsymbol{F_g} = -\frac{\mu_e}{r^3}\boldsymbol{r} + \left(\frac{3J_2\mu_e R_e^2}{2r^5}\begin{bmatrix} r_x(5r_z^2/r^2 - 1) \\ r_y(5r_z^2/r^2 - 1) \\ r_z(5r_z^2/r^2 - 3) \end{bmatrix}\right), \qquad (6)$$

where R_e is the equatorial radius of the Earth, $r = |\boldsymbol{r}|$, μ_e is earth's gravitational parameter, and $J2$ is a constant related to the oblateness of the Earth. To compute the aerodynamic force and torque acting on the spacecraft, the satellite is discretized into a collection of rectangular panels. The aerodynamic force acting at the centroid of each panel under the assumption of specular reflection is calculated by:

$$\boldsymbol{F_p} = -\frac{1}{2}C_p A \rho v_\perp \boldsymbol{v}_\perp, \qquad (7)$$

where C_p is the pressure coefficient, ρ is ambient density, A is the surface area of the panel, and $\boldsymbol{v}_\perp$ is

the projection of the velocity vector relative to the atmosphere $\boldsymbol{v}_\infty$ along the panel normal vector $\hat{\boldsymbol{n}}_{\boldsymbol{p}}$. Density is given by the NRLMSISE-00 model (Picone et al., 2002), which is dependent on the solar and geomagnetic activity as well as the latitude, longitude, altitude, and time. Figure 5 shows the variation in density over time at a given point at a 400 km altitude, highlighting the need for a high-fidelity density model and underscoring the differences in aerodynamic drag force that can occur based on the simulation epoch.

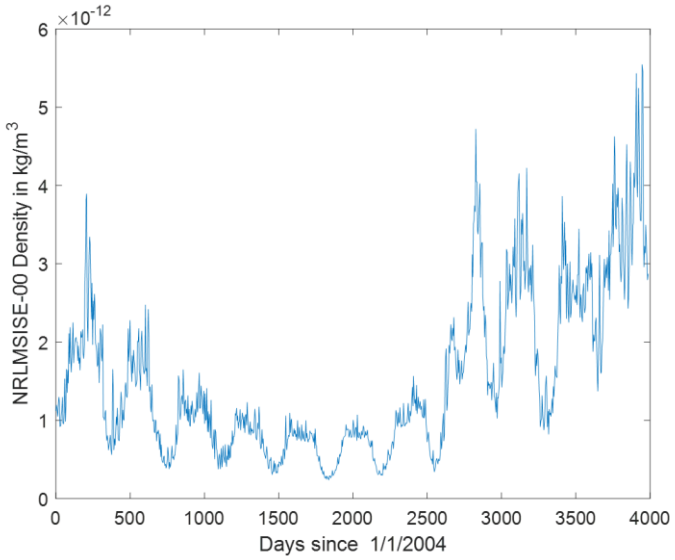

Figure 5. NRLMSISE-00 density over time at ECI position: [-5008.02, 1902.25, 4148.42] km.

When completely specular reflection is assumed, the drag force acting on each panel is perpendicular to the sur- face of the panel and the pressure coefficient is equal to four (Omar and Wersinger, 2014). More advanced aerodynamic models, including specular and diffuse reflections of particles, will be considered in future work (Vallado and Finkleman, 2014). The overarching aerodynamics stability properties of the DMD are not expected to change with the use of these high-fidelity models. If $\boldsymbol{v}_\infty$ and $\hat{\boldsymbol{n}}_{\boldsymbol{p}}$ are more than 90 degrees apart, the panel does not experience any drag force and $\boldsymbol{v}_\perp$ is set to zero. The variables $\boldsymbol{v}_\infty$ and $\boldsymbol{v}_\perp$ are computed as:

$$\boldsymbol{v}_\infty = \boldsymbol{v} - \boldsymbol{\omega_e} \times \boldsymbol{r}, \tag{8}$$

$$\boldsymbol{v}_\perp = \max(\boldsymbol{v}_\infty \cdot \hat{\boldsymbol{n}}_{\boldsymbol{p}}, 0), \tag{9}$$

where $\boldsymbol{\omega_e}$ is the rotation rate of the Earth. If $\boldsymbol{r_p}$ is the vector from the satellite center of mass to the panel centroid, the aerodynamic torque resulting from the panel is:

$$\boldsymbol{\tau_p} = \boldsymbol{r_p} \times \boldsymbol{F_p}. \tag{10}$$

The calculated aerodynamic forces and torques generated by each panel are combined to derive the net aerodynamic force and torque. The spacecraft's attitude, position, and moment of inertia tensor are used to compute the gravity gradient torques with Eq. 3.155 in the work by Markley and Crassidis (2014):

$$\boldsymbol{\tau_{gg}} = \frac{3\mu_e}{r^3}\hat{\boldsymbol{n}} \times (\boldsymbol{J}\hat{\boldsymbol{n}}), \tag{11}$$

where r is the distance from the center of the Earth to the satellite center of mass, $\hat{\boldsymbol{n}}$ is the nadir vector expressed in the spacecraft body frame, and $\boldsymbol{J}$ is the satellite moment of inertia tensor about the center of mass expressed in the spacecraft body frame. Finally, the magnetic torques acting on the satellite are given by Markley and Crassidis (2014) as:

$$\boldsymbol{\tau_{mag}} = \boldsymbol{\mu} \times \boldsymbol{B}, \tag{12}$$

where $\boldsymbol{\mu}$ is the spacecraft magnetic moment vector and $\boldsymbol{B}$ is the Earth's magnetic field vector at the satellite's location.

4. Control Methodology

The satellite will begin in a tumbling state after deployment into space with the DMD booms retracted. At this point, as discussed by Stickler and Alfriend (1976), the BDot de-tumble controller will be activated and the magnetorquers will be used to set the spacecraft magnetic moment to:

$$\boldsymbol{\mu_{bdot}} = -K\dot{\hat{\boldsymbol{B}}} = -K(\hat{\boldsymbol{B}} \times \boldsymbol{\omega}) \approx -K\frac{\hat{\boldsymbol{B}}_2 - \hat{\boldsymbol{B}}_1}{\Delta t}, \tag{13}$$

where K is a user-defined, positive gain and $\dot{\hat{\boldsymbol{B}}}$ is the rate of change of the unit Earth magnetic field vector in the spacecraft body frame as measured by a magnetometer. As shown in Figure 6, the BDot law ensures that the direction of the resulting magnetic torque vector given by Eq. (12) will be as close as possible to $-\boldsymbol{\omega}$, and thus will reduce spacecraft angular velocity to the extent possible for a given magnetic moment magnitude. This can be proven more formally as follows: Substituting Eq. (13) into Eq. (12) gives the magnetic torque vector from the BDot law:

$$\boldsymbol{\tau_{bdot}} = -K\left(\hat{\boldsymbol{B}} \times \boldsymbol{\omega}\right) \times \boldsymbol{B}. \tag{14}$$

The triple vector product rule discussed by Arfken (1985) states that for any three vectors $\boldsymbol{A}, \boldsymbol{B}$, and $\boldsymbol{C}$,

$$(\boldsymbol{A} \times \boldsymbol{B}) \times \boldsymbol{C} = -\boldsymbol{A}(\boldsymbol{B} \cdot \boldsymbol{C}) + \boldsymbol{B}(\boldsymbol{A} \cdot \boldsymbol{C}). \tag{15}$$

Applying this to Eq. (14) yields:

$$\boldsymbol{\tau_{bdot}} = K\hat{\boldsymbol{B}}\left(\omega B\cos(\theta)\right) - K\boldsymbol{\omega}B, \tag{16}$$

where θ is the angle between $\boldsymbol{\omega}$ and $\boldsymbol{B}$. Taking the dot product of Eq. (16) and $\hat{\boldsymbol{\omega}}$ gives the component of $\boldsymbol{\tau_{bdot}}$ along the $\boldsymbol{\omega}$ direction. If this component is negative, then $\boldsymbol{\omega}$ will be reduced in magnitude:

$$\begin{aligned}\boldsymbol{\tau_{bdot}} \cdot \boldsymbol{\omega} &= K\cos(\theta)\left(\omega B\cos(\theta)\right) - K\omega B \\ &= -KB\omega(1-\cos^2(\theta)) \leq 0.\end{aligned} \tag{17}$$

Eq. (17) will be less than zero in all cases except for when θ equals zero. This occurs when the magnetic field is aligned with angular velocity vector, and will result in zero magnetic torque (no reduction in angular velocity). However, because the direction of the magnetic field vector changes along the orbit, a condition with $\theta = 0$ will not persist for any significant time. This ensures that the BDot law will be able to reliably reduce the angular velocity of the satellite.

Optionally, additional logic can be included to scale down the magnitude of $\boldsymbol{\mu_{bdot}}$, when necessary to ensure that the power consumed by the magnetorquers does not exceed a specified threshold P_{max}.

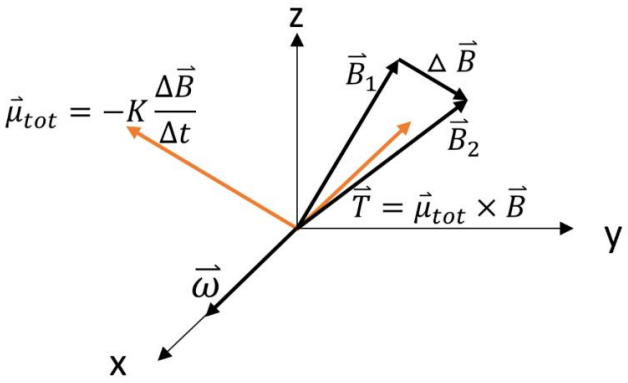

Figure 6. BDot de-tumble controller.

The magnetic moment generated by a magnetorquer is defined by Silani and Lovera (2005) as:

$$\mu_m = I_m A_m n_m, \tag{18}$$

where I_m is the current flowing through the magnetorquer, A_m is the magnetorquer loop area, and n_m is the number of wire loops in the magnetorquer. This magnetic moment vector acts perpendicular to the magnetorquer coil along the direction of the thumb of one's right hand when the fingers are curled in the direction of the current. The electrical power consumed by a magnetorquer is given by:

$$P_m = I_m^2 R_m. \tag{19}$$

For a given $\boldsymbol{\mu_{bdot}}$, the power required from each magnetorquer can be calculated using Eq. (18) and (19) and *a priori* knowledge of A_m, n_m, and R_m for each magnetorquer as:

$$P_{req} = \left(\frac{\mu_m}{A_m n_m}\right)^2 R_m. \tag{20}$$

If the cumulative required magnetorquer power consumption P_{req} would greater than P_{max} the desired BDot magnetic moment vector can be scaled down via the following relation:

$$\boldsymbol{\mu'_{bdot}} = \boldsymbol{u_{bdot}}\sqrt{\frac{P_{max}}{P_{req}}}. \tag{21}$$

The spacecraft magnetic moment vector $\boldsymbol{\mu'_{bdot}}$ will now require power P_{max} to achieve. Because the direction of $\boldsymbol{\mu_{bdot}}$ does not change after this operation, Eq. (17) still holds, and the BDot law will continue to reduce spacecraft angular velocity, as long as $\boldsymbol{B}$ and $\boldsymbol{\omega}$ are not aligned.

In addition to $\boldsymbol{\mu_{bdot}}$, a fixed magnetic moment vector along the desired zenith-pointing satellite axis (in this case, the x-axis in Figure 1), will be superimposed on $\boldsymbol{\mu_{bdot}}$ after de-tumble and partial boom deployment. This fixed magnetic moment will work to align the satellite x-axis with the Earth's magnetic field. At the point in the orbit when the magnetic field (and hence the satellite x-axis) is most-zenith pointing (as determined in advance through orbit propagation), the two DMD booms along the x-axis will be fully deployed and the two booms along the y-axis will be partially deployed. This creates a minimum moment of inertia about the x-axis which gravity gradient torques will naturally align with the zenith vector. Aerodynamic torques will simultaneously align the DMD z-axis (Figure 1) with the velocity vector, resulting in passive three-axis attitude stabilization. All booms can be simultaneously deployed or retracted to facilitate orbital maneuvering while maintaining this attitude stability. Continuing to run the BDot de-tumble controller after boom deployment reduces attitude oscillations and aids in the stability.

5. Simulation Results

5.1. Time Domain Simulations

Figure 7 displays the alignment with respect to the velocity and nadir vectors of a 2U, DMD-equipped CubeSat initially deployed from the International Space Station (circular orbit with inclination of 52 degrees and semi-major axis of 6778 *km*). The simulation epoch occurred on June 5, 2014 at 1200 UTC. In the first 10,000 seconds of the simulation, only the BDot controller is run (retracted booms) with a BDot gain of -5 to de-tumble the satellite. Between t=10,000 and t=20,000 seconds, all booms are deployed to 1 *m* and a fixed magnetic moment of .015 $A*m^2$ along the satellite body frame x-axis is superimposed on the BDot magnetic moment vector.

The $+y$ and $-y$ booms are then deployed to 1.85 m, and the $+x$ and $-x$ booms are deployed to 3.7 m at the point in the next orbit when the magnetic field is most zenith pointing (t=20,656 s). After this, the

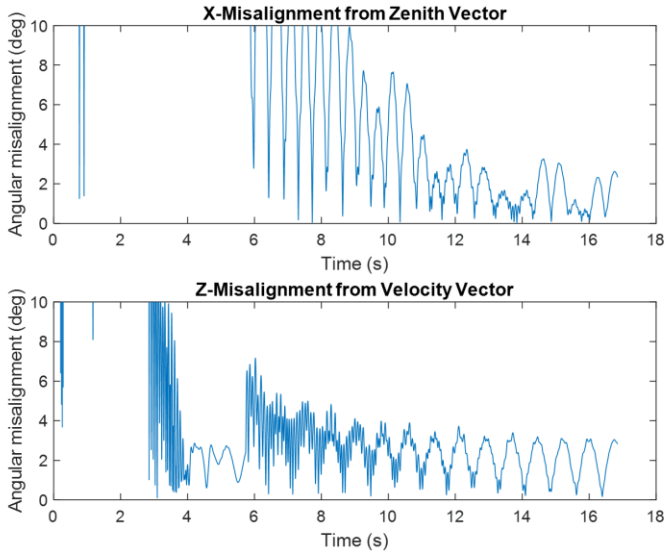

Figure 7. Misalignment between spacecraft x/z axes and zenith/velocity vectors.

fixed magnetic moment is removed, and only the BDot controller continues running to damp attitude oscillations. Note that the attitude oscillations are never completely removed, due to the movement of the zenith and velocity vectors in inertial space over the course of each orbit. The satellite eventually stabilizes with the z-axis aligned with the velocity vector and the x-axis aligned with a steady state pointing error of less than five degrees. Figure 8 shows the error angle between the actual and desired orientation, as well as the spacecraft angular velocity, over time.

Table 2 lists the maximum magnitudes of the gravity gradient, aerodynamic, and magnetic torques over the course of the simulation. While these torques vary throughout the simulation based on the satellite's attitude and position, they are on the order of micro-Newton-meters and achieve their stabilizing effects over a time period of hours. Also note that unlike reaction wheels which produce torques several orders of magnitude greater than the environmental torques, the magnetorquers produce torques of a

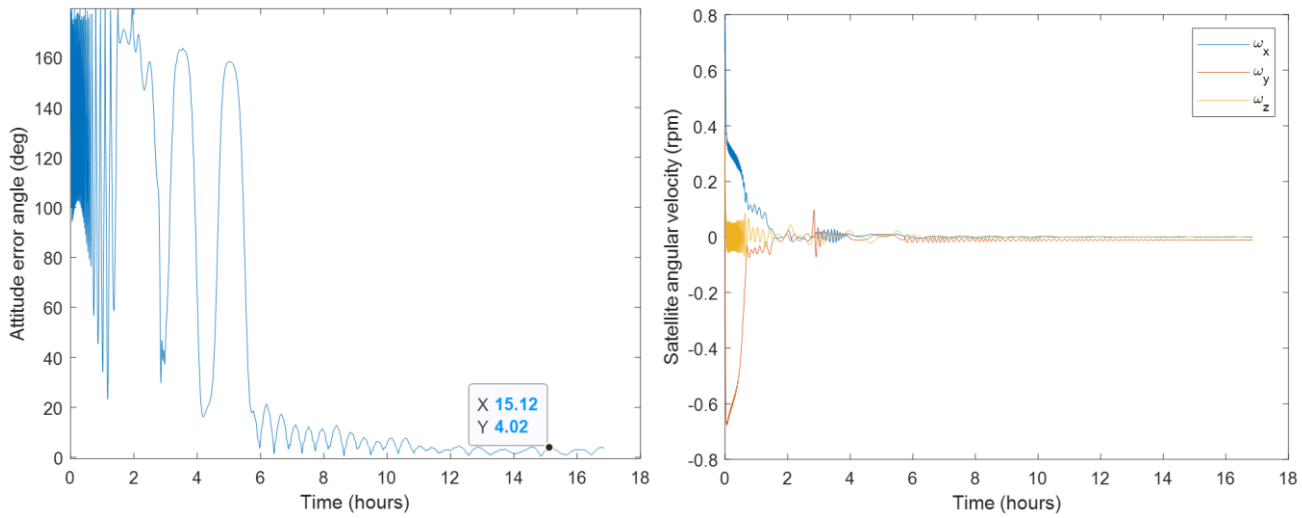

Figure 8. Angle between actual and desired attitude and angular velocity over time in 400 km circular orbit.

similar magnitude to the environmental torques and work in tandem with them to produce a stabilizing effect. Because these torques are so small, a satellite using the DMD for stability must be carefully designed so that disturbance torques caused bymagnetic hysteresis, solar pressure, or solar panel electrical currents do not overwhelm the stabilizing torques. The low magnitudes of the torques acting on the DMD reduce the chance of the DMD booms buckling or oscillating due to dynamic loadings.

Table 2. Maximum Torque Magnitudes for 400 km ISS Orbit

	Gravity Gradient	Aerodynamic	Magnetic
Maximum Torque ($\mu N * m$)	1.06	2.62	1.88

Figure 9 shows the satellite's attitude alignment error over time in a 600 km circular orbit with a 52-degree inclination for epochs of June 5, 2014 (maximum solar activity) and June 5, 2009 (minimum solar activity). Table 3 shows the maximum gravity gradient, aerodynamic, and magnetic torque magnitudes during these simulations. Though the density is lower during the periods of low solar activity and the attitude stability is thus poorer, Figure 9 highlights the ability of the DMD to maintain attitude stability within about 20 degrees even in a minimum density condition at a 600 km altitude. Recall that the desired orientation has the spacecraft z-axis aligned with the velocity vector and x-axis aligned with the zenith vector. The higher the atmospheric density (caused by lower altitudes or greater solar activity), the greater the attitude stability of the DMD-equipped spacecraft. Gravity gradient and magnetic torques are not significantly affected by the orbital altitude or simulation epoch.

Table 3. Maximum Torque Magnitudes for 600 km, 52-degree Inclination Circular Orbits

	Gravity Gradient	Aerodynamic	Magnetic
Maximum Torque, 600 km orbit, solar max ($\mu N * m$)	1.15	1.10	2.15
Maximum Torque, 600 km orbit, solar min ($\mu N * m$)	1.15	.269	1.77

5.2. Boom Failure Analysis

The DMD is relatively robust to the failure of a single boom if the failure is detected and mitigated. If a boom fails at an intermediate length as determined by the rotary encoder contained in each deployer, the opposite boom must be retracted or deployed to the same length so that the configuration remains

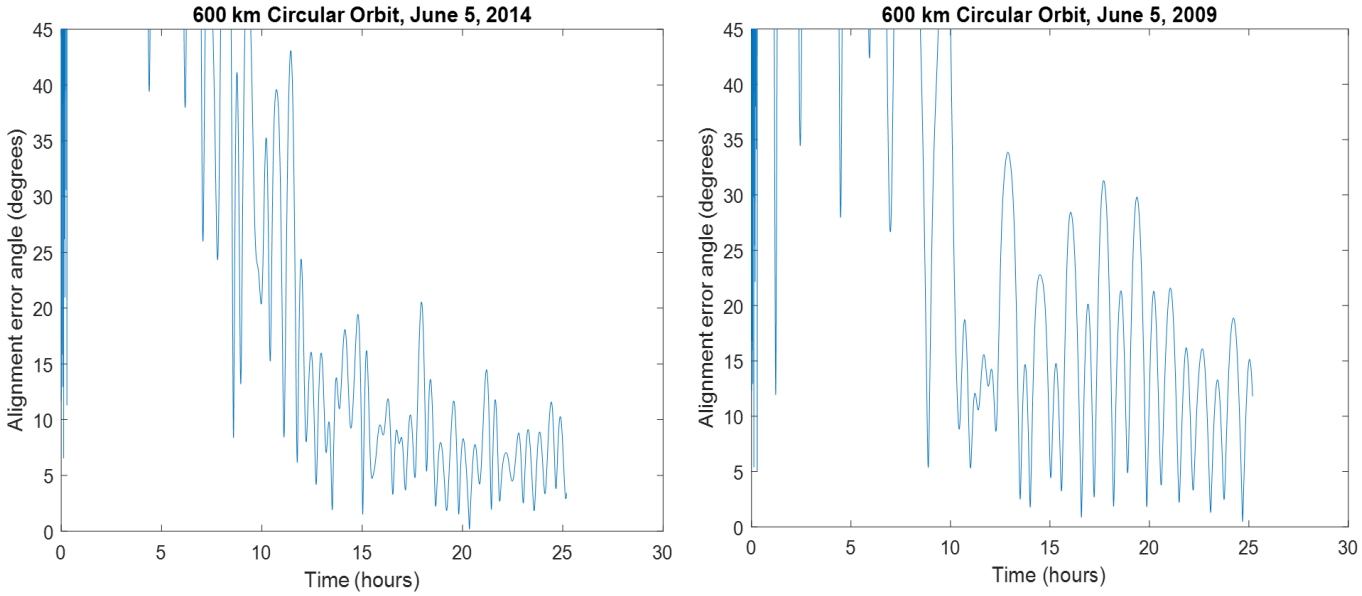

Figure 9. Attitude alignment error over time for 600 km, 52-degree inclined orbits with different epochs.

symmetric. For example, consider a case where the boom most closely aligned with the +y axis gets stuck at .2 m deployment and cannot extend further. In this case, after identifying the failure, the -y boom would be retracted to .2 m as well. With the x-booms fully deployed and the aforementioned magnetorquer control strategy used, the spacecraft would stabilize with the z-axis aligned with the velocity vector and x-axis aligned with the zenith vector. Figure 10 contains the simulation results for this scenario. Although the error angles were higher than in the nominal case (Figure 7), the spacecraft remains stable, despite the boom failure. If one of the booms aligned with the +x or -x axis fails, the satellite can only stabilize in a configuration with the axizs ram-aligned and either the +y or -y axis aligned with the zenith vector.

5.3. Frequency and Flexible Modes Analysis

To ensure that the magnetorquer controller does not excite flexible modes in the booms, the natural frequency of the booms can first be estimated using cantilever beam theory. A Fourier transform on the control signal can then be used to verify that the frequency content of the controller during the time when the booms are deployed is significantly lower than the natural frequency of the booms.

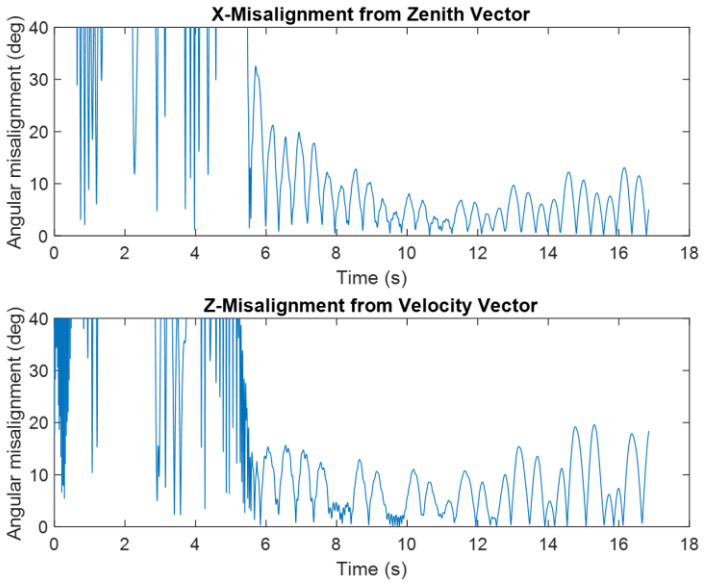

Figure 10. Attitude stabilization when +y boom stuck at .2m deployment

Consider the boom natural frequencies to be approximated by that of a semi-circular cantilever beam made of austenitic 316 stainless steel that is .04 m along the arc, 3.7 m long, .0762 mm thick, and weighing 90 grams. The natural frequency (rad/s) of

a cantilevered beam under a uniform load per unit length w in a gravity field with accel- eration g is given per Roark et al. (2002, Table 16.1) by:

$$\omega_n = K_n\sqrt{\frac{EI_a g}{wl^4}}, \tag{22}$$

where K_n is a constant dependent on the vibrational mode of interest, E is the modulus of elasticity, I_a is the area moment of inertia about the desired bending axis, and l is the length of the beam. Since w is weight per unit length,

$$w = \frac{m_b g}{l}, \tag{23}$$

where m_b is the mass of the boom. Substituting Eq. (23) for w into Eq. (22), and the value of $K_n = 3.52$ which is valid for the first, lowest frequency mode (per Roark et al., 2002, Table 16.1), we get:

$$\omega_n = 3.52\sqrt{\frac{EI_a}{m_b l^3}} \tag{24}$$

for the natural frequency of a cantilever beam of mass m_b and length l. The area moment of inertia of a filled semi-circle with radius r about a line passing through the centroid and parallel to the semi-circle base is:

$$I_{semi} = \left(\frac{\pi}{8} - \frac{8}{9\pi}\right) r^4. \tag{25}$$

If each DMD boom cross-section is approximated as a semi-circular arc of .04 m arc length, the arc radius is: $\frac{.04}{\pi} = .01273$ m. Since the boom is not a solid semi-circle, but is hollow and of small radius, the area moment of inertia can be computed as:

$$I_{boom} = \left(\frac{\pi}{8} - \frac{8}{9\pi}\right)(.01273^4 - (.01273 - 7.62E - 5)^4) = 6.626E - 11. \tag{26}$$

The modulus of elasticity of stainless steel is 193 GPa. From Eq. (24), we can compute the DMD boom natural frequency as:

$$\omega_n = 3.52\sqrt{\frac{193E9(6.626E-11)}{.09(3.7)^3}} = 5.90\,\frac{\text{rad}}{\text{s}} = .94 \text{ Hz}. \tag{27}$$

Using a Fourier transform, the frequency content of the magnetic torque signal during the aforementioned DMD maneuver was computed, as shown in Figure 11. All frequency content of the torque remains well below .09 Hz, which is over an order of magnitude less than the natural frequency of the booms. During initial deployment, when the tumble rate is on the order of 5 deg/s, the control torque frequency is the highest, but is still only .014 Hz. Additionally, the magnitude of the magnetic torque is so tiny that any oscillations observed in the boom will be negligibly small. Because the booms are thin and highly thermally conductive, thermal effects are likewise not expected to induce any significant booms oscillations or cause instability. For this reason, it is a reasonable assumption to treat the spacecraft-DMD assembly as a single rigid body for the purpose of stability assessments.

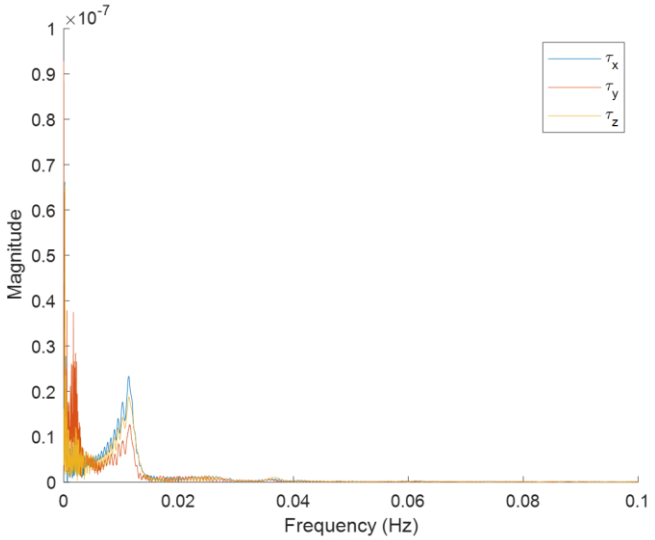

Figure 11. Frequency content of magnetic torque signal during DMD attitude control.

5.4. Monte Carlo Simulations

Monte Carlo simulations were conducted to verify the ability of the DMD to operate at altitudes at and below 600 km in the presence of expected per-

turbations. Unlike conventional spacecraft, where aerodynamic and gravity gradient torques are the primary disturbances, these torques serve to facilitate DMD stability. Solar pressure torque is negligibly small in low Earth orbits and magnetic hysteresis torque is expected to be minimal due to the non-ferro- magnetic nature of the DMD booms. The largest disturbance torque will likely come from parasitic magnetic moments generated by current flow within the solar panels. Simulations assumed a solar-panel-induced parasitic magnetic moment of .004 A*m^2 continuously acting in the x-direction. Roughly 10% of the magnetorquer capability on the simulated DMD CubeSat, .004 A*m^2 is a reasonable value for parasitic magnetic moment on such a satellite. Because stability is always improved at lower altitudes due to the increased aerodynamic forces, all simulation were conducted at an altitude of approximately 600 km with variations in the inclination, right ascension, and true anomaly of the orbit. Epoch was also randomly varied and the satellite was given a random initial attitude and angular velocity. Table 4 shows the values range and probability distributions of the parameters used in the Monte Carlo simulations.

Out of 300 Monte Carlo simulation runs, the satellite stabilized in the proper orientation in 290 cases. Out of these 290 cases, all but one had a final orbit-averaged attitude error of less than 20 degrees. The distribution of these errors is shown in Figure 12; average error was 5.9 degrees relative to the desired attitude for the cases with the correct gravity-gradient orientation. In ten cases, the satellite x-axis ended up stabilizing nadir pointing, instead of zenith pointing, since a gravity gradient configuration is stable in either attitude. If such a case arose in practice, operators could retract the booms and re-run the attitude stabilization procedure. The probability of the satellite stabilizing with the incorrect axis pointing zenith after three such re-runs is 1/27,000.

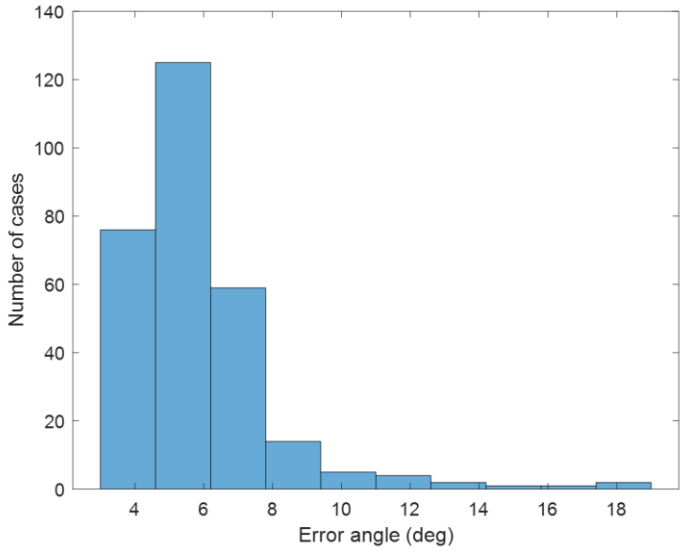

Figure 12. Final orbit averaged angular error relative to desired attitude in Monte Carlo runs at 600 km altitude.

6. Conclusions

The drag maneuvering device is a unique actuator capable of providing simultaneous orbital maneuvering capabilities and semi-passive three-axis attitude stabilization. By independently actuating four tape-spring booms, the DMD can leverage naturally occurring aerodynamic and gravity gradient torques for attitude stability. Embedded magnetorquers are actuated based on magnetometer measurements to damp attitude oscillations and to ensure gravity

Table 4. Monte Carlo Simulation Parameters

Parameter	Value Range	Probability Distribution
Semi-major axis	6978	Constant
Inclination	[52, 90] deg	Uniform
True anomaly	[0, 360] deg	Uniform
Right ascension of ascending node	[0, 360] deg	Uniform
Eccentricity	0	Constant
Quaternion rotation axis (each elem)	[0, 1]	Uniform
Quaternion rotation angle	[0, 360]	Uniform
Angular velocity (each axis)	[-2.9, 2.9] deg/s	Uniform
Epoch	[6/5/2003, 6/5/2014]	Uniform

gradient stabilization in the proper orientation. An attitude control methodology for the DMD was developed in this paper and numerical attitude and orbit simulations verified the attitude stability properties of the DMD. For many Low Earth Orbit satellite missions, particularly for Earth observation and communication, the DMD could entirely replace conventional attitude control and propulsion systems. For example, the DMD could maintain a camera or antenna pointed at the Earth while modulating aerodynamic drag to maintain an orbit slot. This would greatly reduce mission cost while increasing reliability through the use of a simpler system.

Acknowledgments

This work was supported with funds from a NASA Space Technology Research Fellowship, grant number 80NSSC17K0232.

References

Arduini, C. and Baiocco, P. (1997): Active Magnetic Damping Attitude Control for Gravity Gradient Stabilized Spacecraft. *J. of Guidance, Control, and Dynamics*, Vol. 20 (1), pp. 117–122. ISSN: 0731-5090. doi: 10.2514/2.4003. Available at: https://doi.org/10.2514/2.4003 (accessed Jan. 11, 2021).

Arfken, G. (1985): *Triple Scalar Product, Triple Vector Product, in Mathematical Methods for Physicists* (3rd ed., pp. 26–33). Academic Press. ISBN: 978-0-12-384654-9. Available at: https://www.sciencedirect.com/book/9780123846549/mathematical-methods-for-physicists (accessed Jan. 11, 2021).

Bate, R. R., Mueller, D. D., and White, J. E. (1971): *Fundamentals of Astrodynamics*. Dover Publications. ISBN: 978-0-486-60061-1. Available at: https://books.google.com/books/about/Fundamentals_of_Astrodynamics.html?id=UtJK8cetqGkC (accessed Jan. 11, 2021).

Crane, C. and Duffy, J. (2008): *Kinematic Analysis of Robot Manipulators*. Cambridge University Press. ISBN: 0-521-04793-5. Available at: https://www.google.com/books/edition/Kinematic_Analysis_of_Robot_Manipulators/E_VqSTCp7oMC?h1=en&gbpv=0 (accessed Jan. 11, 2021).

Curtis, H. (2009): *Orbital Mechanics for Engineering Students* (2nd ed.). Elsevier. ISBN: 978-0-08-088784-5. Available at: https://www.elsevier.com/books/orbital-mechanics-for-engineering-students/curtis/978-0-12-374778-5 (accessed Jan. 11, 2021).

Guglielmo, D., Omar, S., Bevilacqua, R. et al. (2019): Drag Deorbit Device: A New Standard Reentry Actuator for CubeSats. *AIAA J. of Spacecraft and Rockets*, Vol. 56 (1), pp. 129–145. doi: 10.2514/1.A34218. Available at: https://arc.aiaa.org/doi/10.2514/1.A34218 (accessed Jan. 11, 2021).

Heidt, H., Puig-Suari, J., Moore, J. et al. (2000): CubeSat: A New Generation of Picosatellite for Education and Industry Low-Cost Space Experimentation, in *Proc. 14th Ann. AIAA/USU Conf. on Small Satellites*. AIAA/USU Conf. on Small Satellites, Logan, UT, Aug. 23. Available at: http://digitalcommons.usu.edu/smallsat/2000/All2000/32 (accessed Jan. 11, 2021).

Hodgart, M. (1989): *Gravity Gradient and Magnetorquering Attitude Control for Low-Cost Low Earth Orbit Satellites—The UOSAT Experience*. PhD Thesis, University of Surrey, Dept. of Electrical Engineering. Available at: http://epubs.surrey.ac.uk/844220/1/10148702.pdf (accessed Dec. 20, 2019).

Kumar, R. R., Mazanek, D. D., and Heck, M. L. (1995): Simulation and Shuttle Hitchhiker Validation of Passive Satellite Aerostabilization. *J. of Spacecraft and Rockets*, Vol. 32 (5), pp. 806–811. ISSN: 0022-4650, 1533-6794. doi: https://doi.org/10.2514/3.26688. Available at: http://arc.aiaa.org/doi/abs/10.2514/3.26688 (accessed Jan. 11, 2021).

Lovera, M. (2015): Magnetic Satellite Detumbling: The BDot Algorithm Revisited, in *2015 Am. Control Conf. (ACC)*, pp. 1867–1872. doi: 10.1109/ACC.2015.7171005. Available at: https://ieeexplore.ieee.org/document/7171005 (accessed Jan. 11, 2021).

Markley, F. L. and Crassidis, J. L. (2014): *Fundamentals of Spacecraft Attitude Determination and Control.* Springer-Verlag. ISBN: 978-1-4939-0801-1. Available at: //www.springer.com/us/book/9781493908011 (accessed Jan. 11, 2021).

Mason, J., Baumgart, M., Woods, T. et al. (2016): MinXSS CubeSat On-Orbit Performance and the First Flight of the Blue Canyon Technologies XACT 3- Axis ADCS, in *Proc. of the 30th Ann. AIAA/USU Conf. on Small Satellites*. AIAA/ USU Conf. on Small Satellites, Logan, UT, Aug. 7. AIAA. Available at: https://digitalcommons.usu.edu/small-sat/2016/S5GuidCont/2 (accessed Jan. 11, 2021).

Montenbruck, O. and Gill, E. (2005): *Satellite Orbits* (1st ed.). Springer. ISBN: 978-3-540-67280-7. Available at: https://www.springer.com/de/book/9783540672807 (accessed Jan. 11, 2021).

Omar, S. and Bevilacqua, R. (2019): Guidance, Navigation, and Control Solutions for Spacecraft Re-Entry Point Targeting Using Aerodynamic Drag, in *Acta Astronautica*, Vol. 155, pp. 389–405. ISSN: 0094-5765. doi: 10.1016/j.actaas- tro.2018.10.016. Available at: http://www.sciencedirect.com/ science/article/pii/S0094576518302893 (accessed Jan. 11, 2021).

Omar, S. R. and Wersinger, J. M. (2014): Satellite Formation Control using Differential Drag, in *Proc. of 53rd AIAA Aerospace Sciences Mtg*. 53rd AIAA Aerospace Sciences Mtg., Kissimmee, FL, Jan. AIAA. doi: 10.2514/6.2015-0002. Available at: http://arc.aiaa.org/doi/abs/10.2514/6.2015-0002 (accessed Jan. 11, 2021).

Pastorelli, M., Bevilacqua, R., and Pastorelli, S. (2015): Differential-Drag-based Roto-Translational Control for Propellantless Spacecraft, in *Acta Astronautica*, Vol. 114, pp. 6–21. ISSN: 00945765. doi: https://doi.org/10.1016/j.actaastro.2015.04.014. Available at: http://linkinghub.elsevier.com/retrieve/pii/S0094576515001708 (accessed Jan. 11, 2021).

Pavlis, N. K., Holmes, S. A., Kenyon, S. C. et al. (2012): The Development and Evaluation of the Earth Gravitational Model 2008 (EGM2008). *J. of Geophysical Research: Solid Earth*, Vol. 117 (B4). ISSN: 2156-2202.doi:10.1029/ 2011JB008916. Available at: https:// agupubs.onlinelibrary. wiley.com/doi/abs/10.1029/2011JB008916 (accessed Jan. 11, 2021).

Picone, J. M., Hedin, A. E., Drob, D. P. et al. (2002): NRLMSISE-00 Empirical Model of the Atmosphere: Statistical Comparisons and Scientific Issues. *J. of Geophysical Research: Space Physics*, Vol. 107 (A12), SIA 15-1--SIA 15-16. ISSN: 2156-2202. doi: 10.1029/2002JA009430. Available at: https://agupubs.onlinelibrary.wiley.com/doi/abs/10.1029/2002JA009430 (accessed Jan. 11, 2021).

Roark, R. J., Young, W. C., and Budynas, R. G. (2002): *Roark's Formulas for Stress and Strain* (7th ed). McGraw-Hill. ISBN: 978-0-07-072542-3. Available at: https://www.acessengineeringlibrary.com/content/book/9780071742474 (accessed Jan. 11, 2021).

Roberson, R. E. (1979): Two Decades of Spacecraft Attitude Control. *J. of Guidance, Control, and Dynamics*, Vol. 2 (1), pp. 3–8. ISSN: 0731-5090. doi: 10.2514/ 3.55824. Available at: https://doi.org/10.2514/ 3.55824 (accessed Jan. 11, 2021).

Shrivastava, S. K. and Modi, V. J. (1983): Satellite Attitude Dynamics and Control in the Presence of Environmental Torques—A Brief Survey. *J. of Guidance, Control, and Dynamics*, Vol. 6 (6), pp. 461–471. ISSN: 0731-5090, 1533-3884. doi: 10.2514/3.8526. Available at: http://www.sciencedirect.com/science/article/pii/S0967066103002922 (accessed Jan. 11, 2021).

Silani, E. and Lovera, M. (2005): Magnetic Spacecraft Attitude Control: A Survey and Some New Results. *Control Engineering Practice*, Vol. 13 (3), pp. 357–371. ISSN: 0967-0661. doi: 10.1016/j.conengprac.2003.12.017. Available at: http://www.sciencedirect.com/science/article/pii/S0967066103002922 (accessed Jan. 11, 2021).

Small Spacecraft Systems Virtual Institute (2020): *State of the Art in Small Spacecraft Technology*. (NASA/TP— 2020–5008734). NASA Ames Research Center. Available at: https://www.nasa.gov/sites/default/files/atoms/files/soa2020_final8.pdf. (accessed Dec. 7, 2020).

Steyn, W. and Hashida, Y. (1999): In-orbit Attitude and Orbit Control Commissioning of UoSAT-12, presented at the 4th ESA International Conf. on Spacecraft Guidance, Navigation, and Control Systems (ESTEC), Noordwyk, The Netherlands, Oct. Available at: https://www.researchgate.net/publication/234286824_In-orbit_Attitude_and_Orbit_Control_Commissioning_of-UoSAT-12 (accessed Jan. 11, 2021).

Steyn, W. and Kearney, M.-A. (2014): An Attitude Control System for ZA-Aerosat Subject to Significant Aerodynamic Disturbances, in *Proc. of the 19th World Congress of the Int'l Fed. of Automatic* Control, Vol. 19, pp. 7929–7934. Elsevier. Available at: https://www.sciencedirect.com/science/article/pii/S1474667016428624 (accessed Jan. 11, 2021).

Stickler, A. C. and Alfriend, K. T. (1976): Elementary Magnetic Attitude Control Systems. *J. of Spacecraft and Rockets*, Vol. 13 (5), pp. 282–287. ISSN: 0022-4650. doi: 10.2514/3.57089. Available at: https://arc.aiaa.org/doi/10.2514/3.57089 (accessed Jan. 11, 2021).

Thébault, E., Finlay, C. C., Beggan, C. D. et al. (2015): International Geomagnetic Reference Field: The 12th Generation. *Earth, Planets and Space*, Vol. 67 (1). ISSN: 1880-5981. doi: 10.1186/s40623-015-0228-9. Available at: http://www.earth-planets-space.com/content/67/1/79 (accessed Jan. 11, 2021).

Underwood, C., Viquerat, A., Schenk, M. et al. (2019): InflateSail De-orbit Flight Demonstration Results and Follow-on Drag-sail Applications. *Acta Astronautica*, Vol. 162, pp. 344–358. ISSN: 00945765. doi: 10.1016/j.actaastro.2019.05.054. Available at: https://linkinghub.elsevier.com/retrieve/pii/S0094576519303558 (accessed Jan. 11, 2021).

Vallado, D. A. and Finkleman, D. (2014): A Critical Assessment of Satellite Drag and Atmospheric Density Modeling. *Acta Astronautica*, Vol. 95, pp. 141–165. ISSN: 0094-5765. doi: 10.1016/j.actaastro.2013.10.005. Available at: http://www.sciencedirect.com/science/article/pii/S0094576513003755 (accessed Jan. 11, 2021).

Wie, B. (2008): *Space Vehicle Dynamics and Control* (2nd ed.). AIAA. ISBN: 978-1-56347-953-3, 978-1-60086-011-9. doi: 10.2514/4.860119. Available at: http://arc.aiaa.org/doi/book/10.2514/4.860119 (accessed Jan. 11, 2021).